

Article

Integrated Physical-Constitutive Computational Framework for Plastic Deformation Modeling

Bernhard Viernstein * and Ernst Kozeschnik

Institute of Materials Science and Technology, TU Wien, Getreidemarkt 9, 1060 Vienna, Austria; ernst.kozeschnik@tuwien.ac.at

* Correspondence: bernhard.viernstein@tuwien.ac.at; Tel.: +43-1-58801-308103

Received: 31 March 2020; Accepted: 26 June 2020; Published: 30 June 2020



Abstract: An integrated framework for deformation modeling has been developed, which combines a physical state parameter-based formulation for microstructure evolution during plastic deformation processes with constitutive creep models of polycrystalline materials. The implementations of power law, Coble, Nabarro–Herring and Harper–Dorn creep and grain boundary sliding are described and their contributions to the entire stress response at a virtual applied strain rate are discussed. The present framework simultaneously allows calculating the plastic deformation under prescribed strain rate or constant stress, as well as stress relaxation after preceding stress or strain loading. The framework is successfully applied for the construction of deformation mechanism maps.

Keywords: creep; dislocations; microstructure; relaxation

1. Introduction

The physical understanding of creep mechanisms has been of significant academic interest within the last decades. Especially, the creep response of pure Al has been investigated over a wide temperature and stress range. The physical process of plastic flow is still the subject of controversial discussions for some deformation regimes [1–4], but semi-empirical equations in literature satisfactorily reproduce the experimentally obtained stress-strain relations. The power law regime is associated with vacancy-assisted climb of dislocations, while diffusional flow of atoms is attributed to Coble creep [5] and Nabarro–Herring creep [6]. At low stresses and large grain sizes, Harper–Dorn creep dominates [7–11]. In fine grain structures, grain boundary sliding can control the deformation process [12–16].

In the present work, characteristic creep relations are brought into a homogeneous form and used to calculate the stress response of polycrystalline materials to a constant applied strain rate or the strain rate resulting from an applied external stress load, respectively. Since this framework is based on fundamental plastic deformation mechanisms, thermomechanical simulations are possible for a broad spectrum of metallic materials. Therefore, only characteristic material parameters, which are described in the following discussion, need to be calibrated for each material. Within this work, the model is exemplarily applied to Al. An inverse summation rule of the individual stress contributions ensures that the dominant deformation mechanism mainly defines the overall thermally activated stress response. Microstructural changes during the deformation process are represented by the average dislocation density evolution. The utilized Kocks–Mecking approach considers dislocation generation as well as dynamic and static recovery for dislocation annihilation. The combination of thermally activated stress contributions and the athermal stress contribution from dislocation hardening allows simulating the stress-strain relations over a wide range of temperatures and strain rates. This framework allows for modeling of plastic deformation by dislocation glide as well as of primary creep and secondary creep. The strain rate acceleration and damage accumulation due to cavitation, cracks or both is not

considered, which is typical for tertiary creep. Consequently, this framework is valid for experiments, where creep damage is effectively suppressed, or for materials which show a pronounced secondary creep stage. As an additional feature, stress relaxation tests from literature are successfully simulated within this work to compare the simulation framework with experimental data.

Although not elaborated in the present work, the framework is fully capable of considering microstructural features, such as fine grain hardening, dislocation locking by Cottrell atmospheres or precipitates. Application of the latter two mechanisms has been demonstrated recently by Soliman et al. [17]. These features provide further barriers for ongoing dislocation glide, leading to a higher stress response to an applied strain rate. Diffusion creep, such as Coble creep and Nabarro–Herring creep, are not affected by those microstructural barriers.

2. The model

The following two subchapters describe the implementation of both aspects of this framework, which are the constitutive creep relations on the one hand, and physically-based microstructure evolution on the other hand. A combination of the prevailing stress contribution is presented in Section 3, Results and Discussion.

2.1. Constitutive Modeling of Creep

The deformation characteristics of crystalline materials are mainly controlled by the applied strain rate/external stress loading as well as temperature. Dependent on the particular combination of these parameters, the deformation process is made possible by different physical mechanisms. Generally, at high temperatures, the deformation characteristics show considerable dependency on the applied stress in combination with a low amount of strain hardening. At high temperatures, various creep mechanisms can be operative simultaneously, whereas mostly dislocation glide facilitates plastic deformation at low temperature, high stress or both. Interactions with obstacles, such as grain boundaries, solute atoms, precipitates or other dislocations cause a barrier for an ongoing movement of the mobile dislocations that carry the plastic deformation process. Consequently, the various obstacle strengths determine the rate of dislocation motion and, thus, the strain rate, $\dot{\epsilon}$, which is typically represented by an Arrhenius equation [18–23] as

$$\dot{\epsilon} = \dot{\epsilon}_0 \cdot \exp\left(\frac{-\Delta G}{k_B \cdot T}\right). \quad (1)$$

$\dot{\epsilon}_0$ is a constant [24], k_B the Boltzmann constant, T is the temperature and ΔG is the shear stress-dependent free activation enthalpy, which can be expressed by [20]

$$\Delta G(\sigma_s) = \Delta F \cdot \left[1 - \left(\frac{\sigma_s}{\hat{\tau}}\right)^p\right]^q. \quad (2)$$

ΔF is the total free energy to overcome the obstacle barrier, σ_s the applied shear stress, $\hat{\tau}$ the mechanical threshold, which represents the activation energy barrier in the absence of thermal activation, and p and q define the shape of the energy barrier. In the following, a box shaped barrier is assumed by $p = q = 1$. A combination of Equations (1) and (2) leads to

$$\dot{\epsilon} = \dot{\epsilon}_0 \cdot \exp\left[-\frac{\Delta F}{k_B \cdot T} \cdot \left(1 - \frac{\sigma_s}{\hat{\tau}}\right)\right]. \quad (3)$$

At lower stresses, higher temperatures or both, ($T \geq 0.3 \cdot T_m$), diffusion-controlled deformation regimes, instead of dislocation glide, become dominant. T_m is the melting temperature. Although the

following phenomenological equation does not describe the creep process on a physical basis, it is often successfully applied in literature [20,25,26] and it is also included within this framework as

$$\dot{\epsilon} = \frac{A \cdot D_{tr} \cdot G \cdot b}{k_B \cdot T} \cdot \left(\frac{\sigma_s}{G} \right)^n \quad (4)$$

D_{tr} is the tracer diffusion coefficient of the matrix-forming element, G the shear modulus and b the Burgers vector. Brown and Ashby [26] empirically correlated the coefficients, A and n , based on detailed evaluations of creep data of bcc, fcc, hpc metals (including their alloys), dispersion hardened materials, cubic elements, alkali halides and oxides. Missing explanations for the observed values of n and a huge variety in A of many orders of magnitude motivated Frost and Ashby to include dislocation core diffusion additionally to the bulk matrix diffusion coefficient [20]. Consequently, two rate equations are obtained: At low temperatures or high stresses, dislocation core diffusion is dominant, while lattice diffusion is the dominant mechanism at high temperatures and low stresses. In the following, both mechanisms, which are termed as low-temperature creep, LT creep, and high-temperature creep, HT creep, are dealt with separately. The weighted combination of creep mechanisms is discussed in Section 3. The strain rate, $\dot{\epsilon}_{HT}$, for HT creep can be expressed as

$$\dot{\epsilon}_{HT} = \frac{A_{HT} \cdot G \cdot b \cdot D_{eff}}{k_B \cdot T} \cdot \left(\frac{\sigma_s}{G} \right)^{n_{HT}} \quad (5)$$

n_{HT} is a coefficient and A_{HT} is microstructure-dependent within the present framework (see Section 3). D_{eff} is the effective diffusion coefficient that includes trapping of vacancies at solute atoms [27], excess vacancies [28] and dislocation pipe diffusion [29,30] as inherent diffusion mechanisms. The migration of vacancies predominantly determines diffusion in polycrystalline solids. Here, the creation and annihilation of vacancies at grain boundaries, dislocation jogs or Frank loops are considered within the FSAK model [28]. Additionally, an increasing dislocation density during deformation causes a higher effective diffusion coefficient based on a higher pipe diffusion contribution. The strain rate $\dot{\epsilon}_{LT}$ for the LT creep contribution is calculated as

$$\dot{\epsilon}_{LT} = \frac{A_{LT} \cdot G \cdot b \cdot D_c}{k_B \cdot T} \cdot \left(\frac{\sigma_s}{G} \right)^{n_{LT}} \quad (6)$$

n_{LT} is a constant, A_{LT} is a state-dependent parameter and D_c is the dislocation core diffusion coefficient, which, for Al-based alloys, is given by a correlation with the tracer diffusion coefficient D_{tr} [31]:

$$D_c = 0.11 \cdot \exp\left(\frac{Q_{tr} - Q_c}{R \cdot T}\right) \cdot D_{tr} \quad (7)$$

Q_{tr} and Q_c are the activation energies for bulk diffusion and dislocation core diffusion. R is the universal gas constant. Above a certain stress of approximately $10^{-3}G$, the stress-strain relation typically changes, which is referred to as power law breakdown (PLB). This phenomenon is intensively discussed in literature [32,33]. Within the present framework, the following empirical equation is utilized

$$\dot{\epsilon}_i = \frac{A_i \cdot G \cdot b \cdot D_i}{k_B \cdot T} \cdot \left[\sinh\left(\alpha' \cdot \frac{\sigma_s}{G}\right) \right]^{n_i} \quad (8)$$

$\dot{\epsilon}_i$, A_i , D_i and n_i refer to the prevailing deformation mechanisms and α' specifies the stress level at which the power law break down starts.

At low applied stresses ($\sigma/G < 10^{-5}$) and small grain sizes, diffusional flow determines the deformation process. In contrast to power law creep, strain is caused by the diffusion of vacancies, rather than dislocation mechanisms. This deformation mode has first been described by Nabarro and

Herring [6]. The corresponding creep rate $\dot{\epsilon}_{\text{NH}}$, as implemented within the present framework, is given by [20]

$$\dot{\epsilon}_{\text{NH}} = \frac{42 \cdot b^3 \cdot D_{\text{eff}}}{k_{\text{B}} \cdot T \cdot d^2} \cdot \sigma_{\text{s}}, \quad (9)$$

where d is the grain size. Since lattice diffusion is the predominate mechanism, the effective matrix diffusion coefficient, D_{eff} , is utilized.

Vacancy diffusion along grain boundaries instead of lattice diffusion leads to Coble creep [5]. The strain rate, $\dot{\epsilon}_{\text{C}}$, for Coble creep is formulated as

$$\dot{\epsilon}_{\text{C}} = \frac{42 \cdot b^3 \cdot \pi \cdot \delta \cdot D_{\text{gb}}}{k_{\text{B}} \cdot T \cdot d^3} \cdot \sigma_{\text{s}}. \quad (10)$$

δ is the effective boundary thickness and D_{gb} is the grain boundary diffusion coefficient, which, for Al-based alloys is given [31] as

$$D_{\text{gb}} = 1.4 \cdot \exp\left(\frac{Q_{\text{tr}} - Q_{\text{gb}}}{R \cdot T}\right) \cdot D_{\text{tr}}. \quad (11)$$

Q_{gb} is the activation energy for grain boundary diffusion. At low stresses and large grain sizes, another deformation mechanism occurs, which was first reported by Harper et al. in 1957 [7]. In the following fifty years, the Harper–Dorn regime has been identified in many studies [7–11]. A phenomenological relation between the applied stress, σ_{s} , and the creep rate, $\dot{\epsilon}_{\text{HD}}$, reads

$$\dot{\epsilon}_{\text{HD}} = \frac{A_{\text{HD}} \cdot D_{\text{eff}} \cdot G \cdot b}{k_{\text{B}} \cdot T} \cdot \left(\frac{\sigma_{\text{s}}}{G}\right), \quad (12)$$

where A_{HD} is a coefficient. Equal to the Nabarro–Herring creep, $\dot{\epsilon}_{\text{HD}}$ increases linearly with the applied stress, σ_{s} , (Newtonian nature) and the activation energy is of the magnitude of self-diffusion. However, measured steady-state creep rates of Harper–Dorn creep are often higher by a factor of approximately 1400. Low initial dislocation densities, as well as high purity of the material, favor Harper–Dorn creep, as reported by [4,11]. The low steady-state dislocation density typical for this deformation mechanism remains constant and is independent of σ [8]. A possible explanation is given by the Ardell–Przystupa–Lee (APL) dislocation network theory [1]. The mechanism of the deformation process during Harper–Dorn creep has been discussed intensively in literature [4,7–10] and its analysis is beyond the of scope of this work. Another deformation mechanism, which can control the plastic behavior of fine-grained polycrystalline materials, is based on grain boundary sliding (GBS). Many observations confirm an inverse dependency of the strain rate, $\dot{\epsilon}_{\text{GBS}}$, on squared or cubed grain size [12–16]. If the activation energy is associated with grain boundary diffusion, D_{gb} , the creep rate is [12]:

$$\dot{\epsilon}_{\text{GBS-GB}} = \frac{A_{\text{GBS-GB}} \cdot D_{\text{gb}} \cdot G \cdot b^4}{k_{\text{B}} \cdot T \cdot d^3} \cdot \left(\frac{\sigma}{G}\right)^2, \quad (13)$$

where the coefficient $A_{\text{GBS-GB}} = 2 \cdot 10^5$. If effective lattice diffusion D_{eff} is the rate controlling mechanism, the following equation is utilized [12]:

$$\dot{\epsilon}_{\text{GBS-L}} = \frac{A_{\text{GBS-L}} \cdot D_{\text{eff}} \cdot G \cdot b^3}{k_{\text{B}} \cdot T \cdot d^2} \cdot \left(\frac{\sigma}{G}\right)^2, \quad (14)$$

where the coefficient $A_{\text{GBS-L}} = 8 \cdot 10^6$. The impact of grain boundary sliding processes on conventional Ashby–Frost [20] and Langdon–Mohamed [34,35] deformation mechanism maps are described by Lüthy et al. [12]. It is shown for Ni that D_{gb} - and D_{l} -controlled GBS strongly reduces Coble creep and suppresses Nabarro–Herring creep to insignificant normalized stresses within the Ashby maps. Although Coble creep and Nabarro–Herring creep are overtaken by grain boundary sliding in Al at all

temperatures at an applied normalized stress of $\sigma/G = 10^{-4}$, these mechanisms are incorporated into the framework to achieve a generalized form of all creep mechanisms. Except for the dislocation glide mechanism, all thermally activated deformation processes introduced so far are diffusion-controlled, either by lattice diffusion, pipe diffusion or grain boundary diffusion. The present models describe the activation of dislocation glide, dislocation climb and vacancy diffusion; however, under the assumption of a constant microstructure and no accumulation of creep damage, which is the condition of steady state creep. In real materials, the dislocation density changes during deformation before the steady-state dislocation density is reached. This microstructure evolution is characteristic for the transient range of creep and is discussed in the following.

2.2. Physical Modeling of Microstructure Evolution

For the simulation of the stress evolution during thermomechanical treatments, the knowledge of the current microstructure is mandatory. Therefore, physically based models are utilized, which can simulate the evolution of grain sizes [36,37], nucleation and growth of precipitates, or the current dislocation density. All these models are already implemented within the thermo-kinetic software package MatCalc (<http://matcalc.at>). To incorporate the dislocation strengthening contribution accompanying the transient deformation region, following extended one-parameter model of Kocks and Mecking is used to calculate the temperature and strain rate dependent dislocation density evolution [24]:

$$\frac{d\rho}{d\varepsilon} = \frac{d\rho^+}{d\varepsilon} + \frac{d\rho^-}{d\varepsilon} + \frac{d\rho_s^-}{d\varepsilon} = \frac{M}{bA} \sqrt{\rho} - 2BM \frac{d_{\text{crit}}}{b} \rho - 2CD_d \frac{Gb^3}{\varepsilon kT} (\rho^2 - \rho_{\text{eq}}^2). \quad (15)$$

The Taylor factor, M , relates the macroscopically observed flow stress to the critical resolved shear stress acting on a slip plane within a polycrystalline material. A and B are material-specific coefficients and d_{crit} is the critical annihilation distance between two dislocations [24]. C is a constant and ρ_{eq} is the equilibrium dislocation density. The generation of dislocations $\frac{d\rho^+}{d\varepsilon}$ is caused by dislocation storage in the crystal, being inversely proportional to the current mean distance between dislocations and the dislocation density, ρ , respectively. Annihilation of dislocations occurs by cross slip processes $\frac{d\rho^-}{d\varepsilon}$ at low and intermediate temperatures and by vacancy-assisted climb $\frac{d\rho_s^-}{d\varepsilon}$ at high temperatures. The latter annihilation process represents static recovery, which is marked by the index s . The Taylor equation correlates the athermal, plastic stress contribution with the dislocation density ρ [38,39] as

$$\sigma_p = \alpha \cdot M \cdot b \cdot G \cdot \sqrt{\rho}. \quad (16)$$

The MatCalc software package includes models for the growth and shrinkage of subgrains during plastic deformation, which are out of scope in the present work. The calculation of the average dislocation density for the athermal stress contribution has often been validated [24] and possible industrial applications, such as hot rolling processes, which additionally include recrystallization, have been demonstrated recently [40].

In terms of the possible evolution of the precipitate microstructure, the SFFK model [41–43] is utilized as implemented in the MatCalc software package. Within this framework, a thermodynamic system out of equilibrium state is described by the Gibbs energy, G , given by

$$G = \sum_{i=1}^n N_{0i} \cdot \mu_{0i} + \sum_{k=1}^m \frac{4 \cdot \pi \cdot \rho_k^3}{3} \left(\lambda_k + \sum_{i=1}^n c_{ki} \cdot \mu_{ki} \right) + \sum_{k=1}^m 4 \cdot \pi \cdot \rho_k^2 \cdot \gamma_k. \quad (17)$$

The index i represents the component i in the matrix and the index k represents a specific precipitate with the radius ρ . N_0 is the number of moles, μ_0 the chemical potential, c the concentration and λ accounts for the elastic energy, which is associated with the elastic stress field around the precipitate. γ is the interface free energy density.

The steady-state nucleation rate, J_s , which is defined as the number of formed nuclei per unit volume and unit time, is given by [44,45]

$$J_s = Z \cdot \beta^* \cdot N_C \cdot \exp\left(\frac{-\Delta G^*}{k_B \cdot T}\right), \quad (18)$$

where Z is the Zeldovich factor, β^* the atomic attachment rate, N_C the number of available nucleation sites and ΔG^* is the critical nucleation energy. Equations (17) and (18) provide the basis for rather complex precipitation evolution models, which cause strengthening contributions by shearing- and non-shearing mechanisms. A detailed discussion of precipitation strengthening is beyond the scope of this work and the authors refer to Ahmadi et al. [46]. Solid solution strengthening models as well as the cross core diffusion effect, which can lead to negative strain-rate sensitivity, are implemented in MatCalc and successfully applied, e.g., in Kreyca and Kozeschnik [24]. These thermally activated stress contributions are linked to the present framework by the mechanical threshold $\hat{\tau}$ (Equation (3)). In the following, $\hat{\tau}$ is assumed to remain constant for the benefit of clear discussion.

3. Results and Discussion

In classical creep tests, a constant stress is applied and the resulting creep rate is measured. In an inverse methodology, the creep relations described in the previous section can be utilized to calculate stresses at an applied constant true strain rate. The stress response σ_G of pure dislocation glide is calculated by Equation (3) and leads to

$$\sigma_G = \hat{\tau} \cdot \left(1 - \left[\frac{k_B \cdot T}{\Delta F}\right] \cdot \ln\left(\frac{\dot{\epsilon}}{\dot{\epsilon}_0}\right)\right). \quad (19)$$

Since Equation (19) delivers negative stress values above a certain critical temperature, T_{crit} , the following alternative equation is widely used in literature [24]:

$$\sigma_G = \hat{\tau} \cdot \exp\left(\frac{-k_B \cdot T}{\Delta F} \cdot \ln\left(\frac{\dot{\epsilon}_0}{\dot{\epsilon}}\right)\right). \quad (20)$$

The following equations summarize the present implementation of the LT creep, the HT creep and the Harper–Dorn creep in the integrated framework of deformation modeling. The indices display the different associated pre-factors, A , the diffusion coefficients, D , as well as the exponents, n , with

$$\sigma_i = \left(\frac{k_B \cdot T \cdot \dot{\epsilon}}{A_i \cdot D_i \cdot G \cdot b}\right)^{\frac{1}{n_i}} \cdot G. \quad (21)$$

The power law breakdown regime is implemented with

$$\sigma_i = \sinh^{-1}\left(\frac{k_B \cdot T \cdot \dot{\epsilon}}{A_i \cdot D_i \cdot G \cdot b}\right)^{\frac{1}{n_i}} \cdot \frac{G}{a'}. \quad (22)$$

The stress response of Nabarro–Herring creep, σ_{NH} , and Coble creep, σ_C , are calculated by Equations (9) and (10) and D_{gb} - and D_l -controlled GBS are calculated by Equations (13) and (14). Kreyca [47] has correlated the thermally activated dynamic yield stress contribution at high temperatures with the HT power law creep relation, Equation (5), leading to the relation

$$A_{HT} \propto \frac{\Delta F}{D_{eff} \cdot \hat{\tau}} \cdot \exp\left(\frac{-\Delta F}{R \cdot T}\right), \quad (23)$$

where ΔF is the activation energy for lattice diffusion and D_{eff} is the effective diffusion coefficient. Although it is not very common to connect the mechanical threshold concept $\hat{\tau}$ with the creep behavior,

this approach takes the influence of microstructure features, such as precipitates on the creep rate, into account. It should be emphasized that the particular microstructural state also influences the diffusion coefficient, D_{eff} , of Equation (23) by trapping effects, pipe diffusion or by excess vacancies. For correlating A_{LT} of Equation (6) with the mechanical threshold concept, the core diffusion z as well as the activation energy for pipe diffusion are utilized. This concept is used for calibrating A_{LT} and A_{HT} in the following. Figure 1 shows the Harper–Dorn creep (HD) and power law creep (PL) regime, including the power law breakdown (PLB) at higher stresses. The symbols indicate the normalized strain rate, $\dot{\epsilon} \cdot k_B \cdot T / D_{\text{eff}} \cdot G \cdot b$, as a function of the normalized stress σ / G from Straub and Blum [48] for pure 99.999 Al.

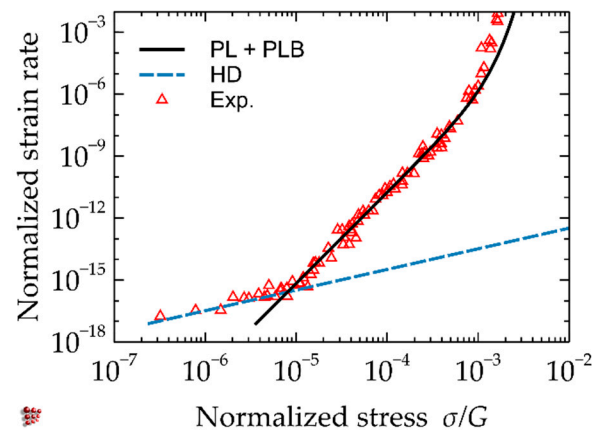


Figure 1. Harper–Dorn creep (HD), power law creep (PL), including power law breakdown (PLB). Symbols indicate experimental results for pure 99.999 Al from [48]. The normalized strain rate is defined by $\dot{\epsilon} \cdot k_B \cdot T / D_{\text{eff}} \cdot G \cdot b$.

All simulation input parameters are listed in Table 1, but instead of $\alpha' = 1000$, which is a typical value in literature [20], better agreement with experimental results are achieved with $\alpha' = 1300$ in this case. In determination of the overall creep behavior, the assumption is made that the creep mechanism with the lowest resulting stress and, therefore, lowest deformation resistance, is dominant. The following summation rule is utilized

$$\left(\frac{1}{\sigma_{\text{ges}}}\right)^{n_c} = \left(\frac{1}{\sigma_G}\right)^{n_c} + \left(\frac{1}{\sigma_{\text{LT}}}\right)^{n_c} + \left(\frac{1}{\sigma_{\text{HT}}}\right)^{n_c} + \left(\frac{1}{\sigma_{\text{NH}}}\right)^{n_c} + \left(\frac{1}{\sigma_C}\right)^{n_c} + \left(\frac{1}{\sigma_{\text{GBS-GB}}}\right)^{n_c} + \left(\frac{1}{\sigma_{\text{GBS-L}}}\right)^{n_c} + \left(\frac{1}{\sigma_{\text{HD}}}\right)^{n_c}, \quad (24)$$

where n_c is the coupling coefficient. The total stress contribution at a certain temperature and strain rate is the sum of the athermal stress contribution, σ_p , of Equation (16) and σ_{ges} of Equation (24). Except for the dislocation glide mechanism, each creep regime is characterized by a linear relation in a double-logarithmic plot until the power law breakdown is reached at high stresses. Exemplary stress-strain rate relations are illustrated in Figure 2 for all discussed deformation regimes at different temperatures from 100 to 500 °C, whereas σ_{ges} of Equation (24) is represented by the bold line, labeled “DYN”. Table 1 lists all simulation input parameters.

The exponent n of the power law mechanism (Equations (5) and (6)) determines the slope of the LT creep and the HT creep range, until the PLB becomes dominant. The Nabarro–Herring creep, the Coble creep and the Harper–Dorn creep deliver parallel shifted results based on the linear relation of stress and strain rate. The slope of the GBS regime is steeper and crosses the Coble creep mechanism at a specific stress value, which depends on the initial grain size, which is 5 μm in this case, and the deformation temperature. At 100 °C, 200 °C and 300 °C, grain boundary diffusion-controlled GBS is dominant at intermediate stress values, which is finally overtaken by dislocation glide (at 100 °C) or high temperature creep (at 200 °C and 300 °C) at high stresses. Above 400 °C, D_1 -controlled GBS replaces D_{gb} -controlled GBS as dominant deformation mode. Figure 2 illustrates that GBS controls

plastic flow in the intermediate stress range, separating diffusional flow and power law creep range, in good agreement with literature [12]. The transition of these deformation regimes is governed by the exponent n_c in Equation (24). The higher the coupling coefficient n_c , the closer is the resulting stress, σ_{ges} , to the prevailing mechanism. A value of $n_c = 10$ is used in the present analysis, which assures that the resulting curves are rather close to the strain rates predicted by the dominating mechanism and numerical artifacts are minimized.

Table 1. Parameters to calculate each deformation regime.

Symbol	Name	Unit	Value	Equation	Source
G	Shear modulus	MPa	$29,438.4-15,052T$	(13), (14), (21), (22)	[49]
b	Burgers Vector	m	$2.86 \cdot 10^{-10}$	(9), (10), (13), (14), (21), (22)	[20]
α	Strengthening coefficient	-	0.34	(16)	[39]
M	Taylor factor	-	3.06	(16)	[24]
ΔF	Activation energy	J/mol	$0.25 \cdot G \cdot b^3$	(19)	[20]
$\dot{\epsilon}_0$	constant	-	$1.46 \cdot 10^5$	(19)	[24]
δ	Effective boundary thickness	m	$2 \cdot 10^{-9}$	(10)	(MatCalc)
d	Grain size	m	$5 \cdot 10^{-6}$	(9), (10), (13), (14)	This work
A_{LT}	LT constant	-	$5.71 \cdot 10^{-13}$	(22)	This work
A_{HT}	HT constant	-	$4.23 \cdot 10^{-7}$	(22)	This work
A_{HD}	HD constant	-	$1 \cdot 10^{-10}$	(21)	[20]
A_{GBS-GB}	D_{GB} -controlled GBS coefficient	-	$2 \cdot 10^5$	(13)	[12]
A_{GBS-L}	D_L -controlled GBS coefficient	-	$8 \cdot 10^6$	(14)	[12]
n_c	coupling coefficient	-	10	(24)	This work
α'	PLB	-	1000	(24)	[20]
n_{LT}	LT exponent	-	6.4	(22)	[20]
n_{HT}	HT exponent	-	4.4	(22)	[20]
n_{HD}	HD exponent	-	1	(21)	[20]
Q_{tr}	Activation energy for bulk diffusion	J/mol	127,200	(7), (11)	[31]
Q_c	Activation energy for dislocation core diffusion	J/mol	83,200	(7)	[31]
Q_{gb}	Activation energy for grain boundary	J/mol	60,200	(11)	[31]

The mechanical threshold, $\hat{\tau}$, which represents the activation energy barrier in the absence of thermal activation, needs to be defined to calculate the dislocation glide contribution, especially at low temperatures (see Equation (20)). Since $\hat{\tau}$ comprises solid solution hardening, precipitation hardening and cross core diffusion hardening (see Section 2.2, Physical modeling of microstructure evolution), the evolution of the microstructure during the deformation processes is inherently included in the integrated model. In the present analysis, no precipitation processes occur in this setup, leading to a constant mechanical threshold $\hat{\tau} = 145$ MPa and consequently, to constants A_{LT} and A_{HT} .

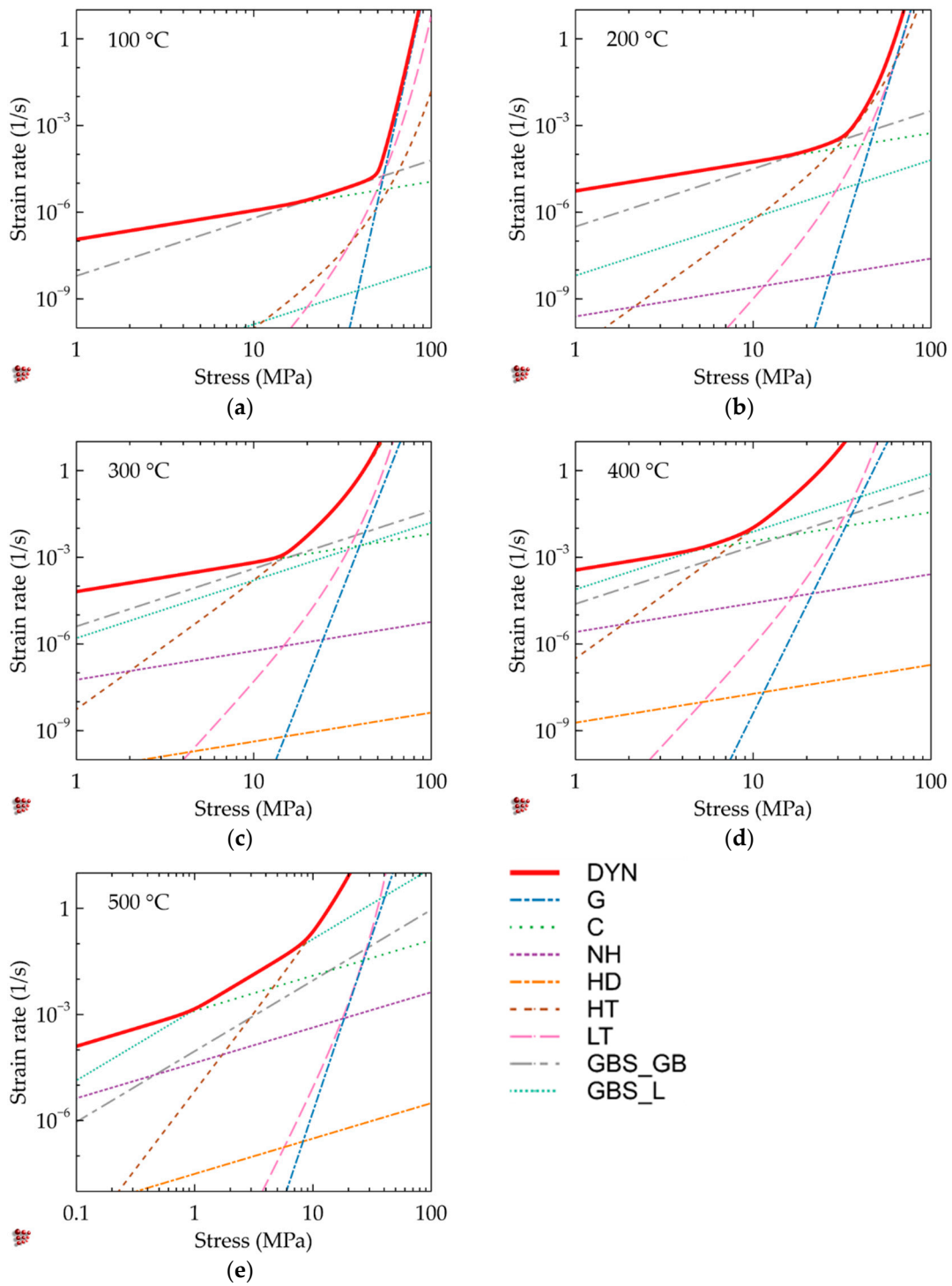


Figure 2. Dislocation glide (G), LT creep (LT), HT creep (HT), Nabarro–Herring creep (NH), Coble creep (C), Harper–Dorn creep (HD), and D_{gb} - and D_1 -controlled GBS (GBS_GB and GBS_L) at different constant strain rates at (a) 100 °C; (b) 200 °C; (c) 300 °C; (d) 400 °C and (e) 500 °C. The resulting stress, σ_{ges} , of Equation (21) is displayed as bold line (DYN).

The present framework allows calculating both, stresses during constant strain rates as well as time-dependent stress relaxation. The stress reduction, $\dot{\sigma}$, during relaxation is assumed to occur along the elastic region with

$$\dot{\sigma} = E \cdot \dot{\epsilon}, \tag{25}$$

where E is the Young's modulus. Hence, the stress reduction, $\dot{\sigma}$, is defined by the current dynamic strain rate, $\dot{\epsilon}$. The new stress value, $\sigma_{t+\Delta t}$, in each iteration step, Δt , of the numerical integration procedure is given by

$$\sigma_{t+\Delta t} = \sigma_t - \dot{\sigma} \cdot \Delta t. \quad (26)$$

For a given materials' microstructure, each stress value corresponds to a unique strain rate, which determines the next stress relaxation step in Equation (25). In this setup, simulations of relaxation tests are carried out. Figure 3a shows relaxation curves of an AlMg4.5Mn alloy, after compressing cylindrical specimens with a constant strain rate of 0.01 (1/s) at different temperatures (350 °C, 400 °C, 450 °C, 500 °C). The experimental points are adopted from the work of Falkinger and Simon [50]. Figure 3b depicts the decreasing strain rate during the relaxation process, starting from 0.01 (1/s). The higher the deformation temperature in the pre-step, the lower the initial stress level for relaxation is, resulting in lower strain rates. The stress reduction of the HT creep (HT), the LT creep (LT), the Coble creep, lattice diffusion controlled GBS as well as grain boundary diffusion-controlled GBS are illustrated for 350 °C in Figure 3c and 500 °C in Figure 3d. According to Equation (24), Nabarro–Herring and Harper–Dorn creep are negligible in this example setup, due to their exceeding stress contributions. The calibration settings are summarized in Table 1, but $A_{HT} = 2.15 \cdot 10^{-11}$ and $A_{LT} = 5.71 \cdot 10^{-17}$ for this specific alloy. Usually, A_{HT} and A_{LT} are calibrated by conventional creep tests instead of relaxation tests. The aim of Figure 3 is to illustrate the possibility of calculating stress relaxations within this framework for a specific set of parameters. When the stress relaxation starts after compressing the cylinder, HT creep controls the plastic flow at 350 °C and 500 °C, as shown in Figure 3c,d at 0 s. As the strain rate rapidly decreases in both cases, lattice diffusion-controlled GBS becomes the dominant mechanism. At very low stresses and strain rates, Coble creep becomes the dominant mechanism at 500 °C. The total thermal stress contribution, σ_{ges} , of Equation (24) is named "DYN" in Figure 3c,d. The athermal stress contributions at the high temperatures and small strain rates (Equation (16)) are not significant due to a negligible amount of dislocation generation.

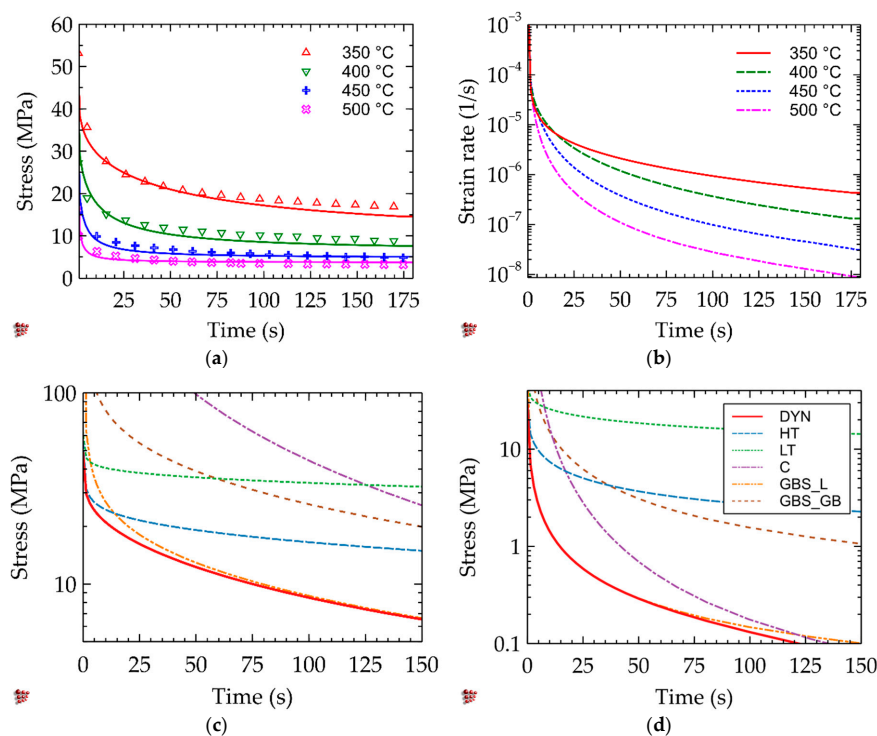


Figure 3. (a) Relaxation tests of an AlMg4.5Mn aluminum alloy at different temperatures. The solid lines are the simulations, whereas the symbols indicate the experimental results from [50]; (b) logarithmic strain rate reduction; logarithmic stress calculations of HT creep (HT), LT creep (LT), Coble creep, D_{gb} - and D_1 -controlled GBS and the total thermal stress contribution (DYN) (c) at 350 °C and (d) at 500 °C.

An additional possible application of this framework is the construction of deformation maps, which provide information about the dominant deformation mechanism at specific temperatures and applied shear stresses. Figure 4 shows the calculated normalized stresses (σ/G) for different strain rates and temperatures in dependence of the grain diameter ((a) 5 μm , (b) 50 μm) for pure Al. Since grain rotation is not considered in the present work, application of the framework to sub-micrometer grain sizes might deliver inaccurate results (ultra-fine grained materials). The numbers in Figure 4 denote the corresponding deformation mechanisms and the black, bold lines indicate the transitions between the different deformation regimes.

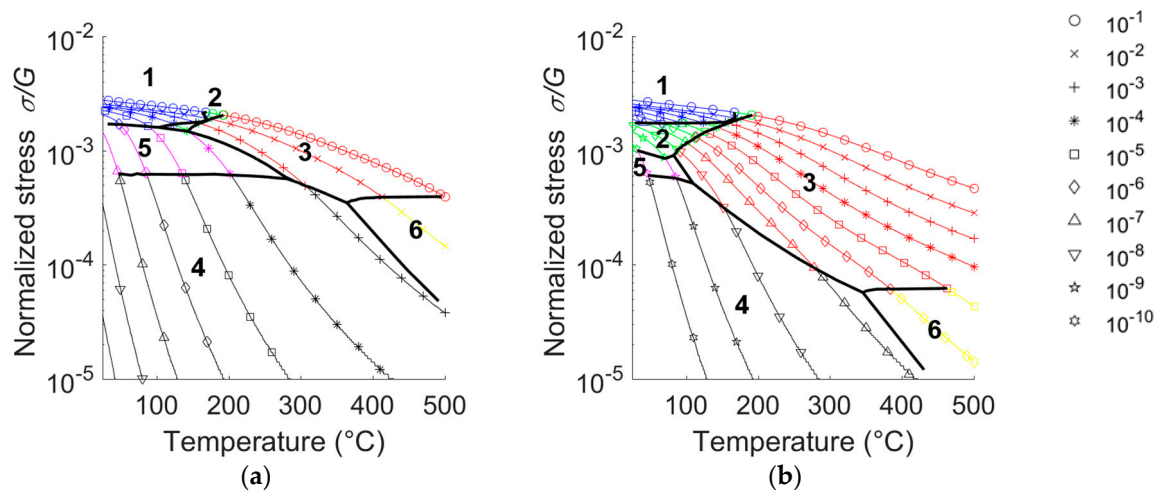


Figure 4. Exemplary deformation maps for pure Al. Normalized stress [-] for different temperatures and strain rates for (a) 5 μm and (b) 50 μm . The black, bold lines indicate transitions between the deformation regimes. The numbers indicate the dominant deformation mechanisms: dislocation glide (1); LT creep (2); HT creep (3); Coble creep (4); D_{gb} -controlled GBS (5) and D_1 -controlled GBS (6).

Figure 4 shows representative deformation maps that have been generated without explicit calibration and thus they allow only for qualitative and exemplary analysis. In this sense, Figure 4a illustrates that GBS becomes the deformation-controlling mechanism at small grain sizes for a wide temperature range, which is in good agreement with literature [12]. Increasing GBS-fields are accompanied by shrinking LT creep and HT creep fields within the deformation maps. The dislocation density rapidly increases at high strain rates, leading to an increasing pipe diffusion coefficient, D_C , and a larger LT creep field (number 2). A detailed description of deformation maps and a catalogue of maps for various groups of materials are provided by Frost and Ashby [20]. The effects of GBS on Frost–Ashby deformation maps are discussed in [12].

4. Conclusions

The implementation of creep mechanisms and their contributions to the stress response to an applied strain rate within an integrated framework for deformation modeling is discussed. Although, steady state is usually presumed for the secondary creep relations under no creep damage condition, athermal dislocation strengthening contribution and the mechanical threshold concept are considered. In the present framework, an integration of the influence of precipitates on the creep regimes is possible but was beyond the scope of this work. It is demonstrated that plastic flow is either governed by dislocation glide, diffusion of either vacancies or dislocations or by grain boundary sliding. The effective diffusion coefficient, which is influenced by pipe diffusion enhancement, excess vacancies or trapping effects, is accounted for. This new framework allows calculating the creep or plastic deformation behavior, while applying either a constant stress, stress relaxation after previous deformation or constant strain rate loading. Exemplary deformation maps for Al are calculated with the present model. Considering the microstructure evolution within a wide range of temperature and strain rate

makes this framework suitable for many industrial applications, such as hot forming processes or strain relaxation during stress relieve annealing.

Author Contributions: Methodology, B.V.; software, B.V. and E.K.; investigation, B.V.; writing—original draft preparation, B.V.; writing—review and editing, E.K.; visualization, B.V.; supervision, E.K.; All authors have read and agreed to the published version of the manuscript.

Funding: This research received no external funding.

Acknowledgments: The authors acknowledge TU Wien Bibliothek for financial support through its Open Access Funding Program.

Conflicts of Interest: The authors declare no conflict of interest.

References

1. Ardell, A.J. Harper-Dorn creep—The dislocation network theory revisited. *Scr. Mater.* **2013**, *69*, 541–544. [[CrossRef](#)]
2. Kumar, P.; Kassner, M.E.; Langdon, T.G. Fifty years of Harper-Dorn creep: A viable creep mechanism or a Californian artifact? *J. Mater. Sci.* **2007**, *42*, 409–420. [[CrossRef](#)]
3. Blum, W.; Maier, W. Harper-Dorn Creep—A Myth? *Phys. Stat. Sol.* **1999**, *467*, 467–474. [[CrossRef](#)]
4. Mohamed, F.A. Harper-Dorn creep: Controversy, requirements, and origin. *Mater. Sci. Eng. A* **2007**, *463*, 177–184. [[CrossRef](#)]
5. Coble, R.L. A Model for Boundary Diffusion Controlled Creep in Polycrystalline Materials. *J. Appl. Phys.* **1963**, *34*, 1679–1682. [[CrossRef](#)]
6. Herring, C. Diffusional viscosity of a polycrystalline solid. *J. Appl. Phys.* **1950**, *21*, 437–445. [[CrossRef](#)]
7. Harper, J.G.; Shepard, L.A.; Dorn, J.E. Creep of aluminum under extremely small stresses. *Acta Metall.* **1958**, *6*, 509–518. [[CrossRef](#)]
8. Yavari, P.; Miller, D.A.; Langdon, T.G. An investigation of harper-dorn creep-I. Mechanical and microstructural characteristics. *Acta Metall.* **1982**, *30*, 871–879. [[CrossRef](#)]
9. Kassner, M.E.; Kumar, P.; Blum, W. Harper-Dorn creep. *Int. J. Plast.* **2007**, *23*, 980–1000. [[CrossRef](#)]
10. Ruano, O.A.; Wadsworth, J.; Sherby, O.D. Harper-dorn creep in pure metals. *Acta Metall.* **1988**, *36*, 1117–1128. [[CrossRef](#)]
11. Barrett, C.R.; Nix, W.D. High Temperature-Low Stress Creep of Al and Al + 0.5% Fe. *Mater. Sci. Eng.* **1972**, *10*, 33–42. [[CrossRef](#)]
12. Lüthy, H.; White, R.A.; Sherby, O.D. Grain boundary sliding and deformation mechanism maps. *Mater. Sci. Eng.* **1979**, *39*, 211–216. [[CrossRef](#)]
13. Ruano, O.A.; Miller, A.K.; Sherby, O.D. The influence of pipe diffusion on the creep of fine-grained materials. *Mater. Sci. Eng.* **1981**, *51*, 9–16. [[CrossRef](#)]
14. Hayden, H.W.; Floreen, S.; Goodell, P.D. Deformation mechanisms of superplasticity. *Met. Trans.* **1972**, *3*, 833–842. [[CrossRef](#)]
15. Alden, T.H. The origin of superplasticity in the sn-5%bi alloy. *Acta Metall.* **1967**, *15*, 469–480. [[CrossRef](#)]
16. Herriot, G.; Suery, M.; Baudalet, B. Superplastic behaviour of the industrial Cu7wt.%P ALLOY. *Scr. Metall.* **1972**, *6*, 657–662. [[CrossRef](#)]
17. Soliman, M.; Shan, Y.V.; Mendez-Martin, F.; Kozeschnik, E.; Palkowski, H. Strain Aging Characterization and Physical Modelling of Over-Aging in Dual Phase Steel. *Mater. Sci. Eng. A* **2020**, *788*, 139595. [[CrossRef](#)]
18. Kocks, U.F. Laws for work hardening and low temperature creep.pdf. *J. Eng. Mater. Technol.* **1976**, *98*, 76–85. [[CrossRef](#)]
19. Follansbee, P.S.; Kocks, U.F. A constitutive description of the deformation of copper based on the use of the mechanical threshold stress as an internal state variable. *Acta Metall.* **1988**, *36*, 81–93. [[CrossRef](#)]
20. Frost, H.J.; Ashby, M.F. *Deformation-Mechanism Maps, The Plasticity and Creep of Metals and Ceramics*, 1st ed.; Pergamon Press: Oxford, UK, 1982.
21. Schoeck, G. The Activation Energy of Dislocation Movement. *Phys. Stat. Sol.* **1965**, *8*, 499–507. [[CrossRef](#)]
22. Argon, A.S. *Mechanical Properties of Single-Phase Crystalline Media: Deformation at Low Temperatures*, 4th ed.; Elsevier B.V.: Amsterdam, The Netherlands, 1996.

23. Schulze, V.; Voehringer, O. Influence of Alloying Elements on the Strain Rate and Temperature Dependence of the Flow Stress of Steels. *Metall. Mater. Trans. A* **2000**, *31*, 825–830. [[CrossRef](#)]
24. Kreyca, J.; Kozeschnik, E. State parameter-based constitutive modelling of stress strain curves in Al-Mg solid solutions. *Int. J. Plast.* **2018**, *103*, 67–80. [[CrossRef](#)]
25. Walser, B.; Sherby, O.D. The Structure dependence of power law creep. *Scr. Metall.* **1982**, *16*, 213–219. [[CrossRef](#)]
26. Brown, A.M.; Ashby, M.F. On the power-law creep equation. *Scr. Metall.* **1980**, *14*, 1297–1302. [[CrossRef](#)]
27. Fischer, F.D.; Svoboda, J.; Kozeschnik, E. Interstitial diffusion in systems with multiple sorts of traps. *Model. Simul. Mater. Sci. Eng.* **2013**, *21*, 025008. [[CrossRef](#)]
28. Fischer, F.D.; Svoboda, J.; Appel, F.; Kozeschnik, E. Modeling of excess vacancy annihilation at different types of sinks. *Acta Mater.* **2011**, *59*, 3463–3472. [[CrossRef](#)]
29. Radis, R.; Kozeschnik, E. Numerical simulation of NbC precipitation in microalloyed steel. *Model. Simul. Mater. Sci. Eng.* **2012**, *20*, 055010. [[CrossRef](#)]
30. Dutta, B.; Palmiere, E.J.; Sellars, C.M. Modelling the kinetics of strain induced precipitation in Nb microalloyed steels.pdf. *Acta Mater.* **2001**, *49*, 785–794. [[CrossRef](#)]
31. Stechauner, G.; Kozeschnik, E. Assessment of substitutional self-diffusion along short-circuit paths in Al, Fe and Ni. *Calphad Comput. Coupling Phase Diagr. Thermochem.* **2014**, *47*, 92–99. [[CrossRef](#)]
32. Jonas, J.J. The back stress in high temperature deformation. *Acta Metall.* **1969**, *17*, 397–405. [[CrossRef](#)]
33. Wong, W.A.; Jonas, J.J. Aluminum Extrusion as a Thermally Activated Process. *Met. Soc. AIME Trans.* **1968**, *242*, 2271–2280.
34. Langdon, T.G.; Mohamed, F.A. A new type of deformation mechanism map for high-temperature creep. *Mater. Sci. Eng.* **1978**, *32*, 103–112. [[CrossRef](#)]
35. Mohamed, F.A.; Langdon, T.G. Deformation Mechanism Maps Based on Grain Size. *Met. Trans.* **1974**, *5*, 2339–2345. [[CrossRef](#)]
36. Maalekian, M.; Radis, R.; Militzer, M.; Moreau, A.; Poole, W.J. In situ measurement and modelling of austenite grain growth in a Ti/Nb microalloyed steel. *Acta Mater.* **2012**, *60*, 1015–1026. [[CrossRef](#)]
37. Cha, S.C.; Hong, S.-H.; Kim, M.-Y.; Park, J.; Shim, J.-H.; Jung, W.-S.; Rath, M.; Kozeschnik, E. CALPHAD-based alloy design for advanced automotive steels—Part II: Compositional and microstructural modification for advanced carburizing steels. *Calphad Comput. Coupling Phase Diagr. Thermochem.* **2016**, *54*, 172–180. [[CrossRef](#)]
38. Taylor, G.I. The Mechanism of Plastic Deformation of Crystals. Part I. *Theoretical. Proc. R. Soc. A Math. Phys. Eng. Sci.* **1934**, *145*, 362–387.
39. Sauzay, M.; Kubin, L.P. Scaling laws for dislocation microstructures in monotonic and cyclic deformation of fcc metals. *Prog. Mater. Sci.* **2011**, *56*, 725–784. [[CrossRef](#)]
40. Buken, H.; Kozeschnik, E. State parameter-based modelling of microstructure evolution in micro-alloyed steel during hot forming. *IOP Conf. Ser. Mater. Sci. Eng.* **2016**, *119*, 012023. [[CrossRef](#)]
41. Svoboda, J.; Fischer, F.D.; Fratzl, P.; Kozeschnik, E. Modelling of kinetics in multi-component multi-phase systems with spherical precipitates I: Theory. *Mater. Sci. Eng. A* **2004**, *385*, 166–174.
42. Kozeschnik, E.; Svoboda, J.; Fratzl, P.; Fischer, F.D. Modelling of kinetics in multi-component multi-phase systems with spherical precipitates II: Numerical solution and application. *Mater. Sci. Eng. A* **2004**, *385*, 157–165.
43. Kozeschnik, E.; Svoboda, J.; Fischer, F.D. Modified evolution equations for the precipitation kinetics of complex phases in multi-component systems. *Calphad Comput. Coupling Phase Diagr. Thermochem.* **2004**, *28*, 379–382. [[CrossRef](#)]
44. Russell, K.C. Nucleation in solids: The induction and steady state effects. *Adv. Colloid Interface Sci.* **1980**, *13*, 205–318. [[CrossRef](#)]
45. Kozeschnik, E. *Modeling Solid-State Precipitation*; Momentum Press LLC: New York, NY, USA, 2013.
46. Ahmadi, M.R.; Povoden-Karadeniz, E.; Öksüz, K.I.; Falahati, A.; Kozeschnik, E. A model for precipitation strengthening in multi-particle systems. *Comput. Mater. Sci.* **2014**, *91*, 173–186. [[CrossRef](#)]
47. Kreyca, F.J. *State Parameter Based Modelling of Stress-Strain Curves in Aluminium Alloys*; TU Wien: Vienna, Austria, 2017.
48. Straub, S.; Blum, W. Does the natural third power law of steady state creep hold for pure aluminium. *Scr. Metall. Mater.* **1990**, *24*, 1837–1842. [[CrossRef](#)]

49. Galindo-Nava, E.I.; Sietsma, J.; Rivera-Díaz-Del-Castillo, P.E.J. Dislocation annihilation in plastic deformation: II. Kocks-Mecking Analysis. *Acta Mater.* **2012**, *60*, 2615–2624. [[CrossRef](#)]
50. Falkinger, G.; Simon, P. Static recovery of an AlMg4.5Mn aluminium alloy during multi-pass hot-rolling. *Procedia Eng.* **2017**, *207*, 31–36. [[CrossRef](#)]



© 2020 by the authors. Licensee MDPI, Basel, Switzerland. This article is an open access article distributed under the terms and conditions of the Creative Commons Attribution (CC BY) license (<http://creativecommons.org/licenses/by/4.0/>).